Body stiffness in orthogonal directions oppositely affects worm-like robot turning and straight-line locomotion

A Kandhari[1], Y Huang[1], K A Daltorio[1], H J Chiel[2, 3, 4] and R D Quinn[1]

[1]*Department of Mechanical and Aerospace Engineering, Case Western Reserve University, Cleveland, Ohio, USA*

Departments of [2]*Biology,* [3]*Neurosciences, and,* [4]*Biomedical Engineering, Case Western Reserve University, Cleveland, Ohio, USA*

E-mail: akhil.kandhari@case.edu

Abstract: Earthworms locomote using traveling waves of segment contraction and expansion, which when symmetric result in straight-line locomotion and when biased result in turning. The mechanics of the soft body permit a large range of possible body shapes which both comply with the environment and contribute to directed locomotion. Inspired by earthworms, our new platform Compliant Modular Mesh Worm robot with Steering (CMMWorm-S) has been developed to study this type of locomotion. Compared with our previous robots, CMMWorm-S is capable of an entirely new movement (turning) using two actuated degrees of freedom per segment (a total of 12 motors). The modularity of the mesh, composed of 3D printed rigid pieces and flexible tubes, allows for the interchange of components to vary the stiffness of the robot. On this robotic platform, we show that locomotion efficiency is sensitive to body stiffness. In particular, greater bending stiffness improves turning locomotion, whereas greater circumferential stiffness speeds straight-line locomotion. The data presented demonstrate the contribution of each component towards the longitudinal, circumferential and bending stiffness of mesh-based robots. These analyses can help in the development of design criteria useful for future soft robotic peristaltic devices.

1. Introduction

Developing soft-bodied robots capable of animal-like locomotion is a challenging problem and biological insights could be valuable for both mechanical design and control strategies. Soft-bodied animals, such as earthworms, can locomote in diverse environments. Their soft bodies allow them to squeeze through confined spaces, comply with their environment and make sharp turns. Duplicating these behaviors for robotics would be valuable in constrained-space applications (such as burrowing, exploration and search and rescue). Navigating these challenging environments may require new combinations of compliant and stiff structural elements.

Inspired by soft-bodied animals such as earthworms, many researchers are developing soft robots (Rus and Tolley 2015, Kim et al 2013). Locomotion techniques based on animals such as worms (Omori et al 2010), caterpillars (Umedachi and Trimmer 2014), snakes (Onal and Rus, 2012), and snails (Chan et al 2007) have been useful in navigating constrained environments. Applications include inspection of pipes (Ikeuchi et al

2012, Harigaya et al 2013), search and rescue (Trimmer et al 2006), exploration (Bertetto and Ruggiu 2001, Omori et al 2009, Tanaka et al 2014) and endoscopy (Mangan et al 2002, Dario et al 2004, Wang and Yan 2007).

Many different worm-like robots have been constructed using a variety of actuators. These robots often have large numbers of kinematically redundant degrees of freedom and are termed hyper-redundant (Chirikjian and Burdick 1991, Trivedi et al. 2008). Compressed air was used to actuate our (Mangan et al. 2002) and Dario's (Dario et al, 2004) endoscopic robots. Both were shown to locomote through constrained spaces. These robots rely on their body softness that allows the structure to comply with their surroundings in order to navigate constrained environments. Shape memory alloys (SMAs) actuate Meshworm (Seok et al 2013), inspired by earthworms, and 3D-PS Robot (Umedachi et al 2014), inspired by caterpillars. These robots are highly deformable and can locomote on a planar surface. Servomotors actuate flexible-type robots (Omorio et al. 2010), inspired by earthworms, to mimic peristaltic locomotion and move in curved tubes using an active turning mechanism. A single DC motor actuates our Softworm (Boxerbaum et al 2010) robot, which is made of a continuously deformable mesh that uses cables for actuation. The single motor turning a cam generates smooth waves of cable tension causing continuous peristaltic locomotion.

Whereas worm-like peristalsis has been shown to be effective for forward locomotion in worm-inspired robots, effective navigation in real-world environments requires being able to make volitional turns. Earthworms and other soft-bodied animals most commonly turn their bodies by small angles by forming low amplitude bends along their body lengths (Kim et al 2011). Adding steering to a worm robot permits volitional control and allows for movement in more complex environments. Soft-bodied robots achieve turning in different ways. For example, earthworm-inspired robots have turned by varying segment lengths using servomotors, (Omori et al 2008), by using shape memory alloys (SMA) that bend the segment about pivot points (Umedachi and Trimmer 2014), or by adding additional SMAs along the longitudinal axis (Seok et al 2013).

Previous investigators have not explored relationships between body stiffness, circumferential stiffness and the effectiveness of locomotion and turning. In this paper, we explore worm-inspired biomechanical and control strategies for forward locomotion and turning using peristalsis on a new robotic platform. In particular, we empirically determine the relative roles of circumferential, longitudinal and bending stiffness for forward locomotion and turning. Based on these measurements, we present a stiffness model that can be used in the design of future soft robots.

To investigate worm-like turning in a soft-bodied robot, we designed and constructed a new robot: Compliant Modular Mesh Worm with Steering (CMMWorm-S). Unlike its predecessor, CMMWorm-O (Horchler et al 2015b), this new robot has two motors in each of its six segments that allow for differential strain in a segment, which results in turning of the robot. The new robot's modularity allows us to easily interchange components to alter different stiffness characteristics of the robot. To understand how compliant components affect longitudinal, circumferential and bending stiffness, tubes of different bending stiffness values and return springs of different stiffnessess are implemented and the gross stiffness properties of the robot are measured. Peristaltic locomotion tests are also conducted on flat ground for both straight-line locomotion and turning to analyze how different stiffness values affect performance of worm robots. As a result, we report that greater bending stiffness improves turning locomotion, whereas greater circumferential stiffness speeds straight-line locomotion.

2. CMMWorm-S Robot Design

CMMWorm-S (figure 1) has two motors (instead of the one in our previous robot) in each of its six segments to allow for differential peristalsis.
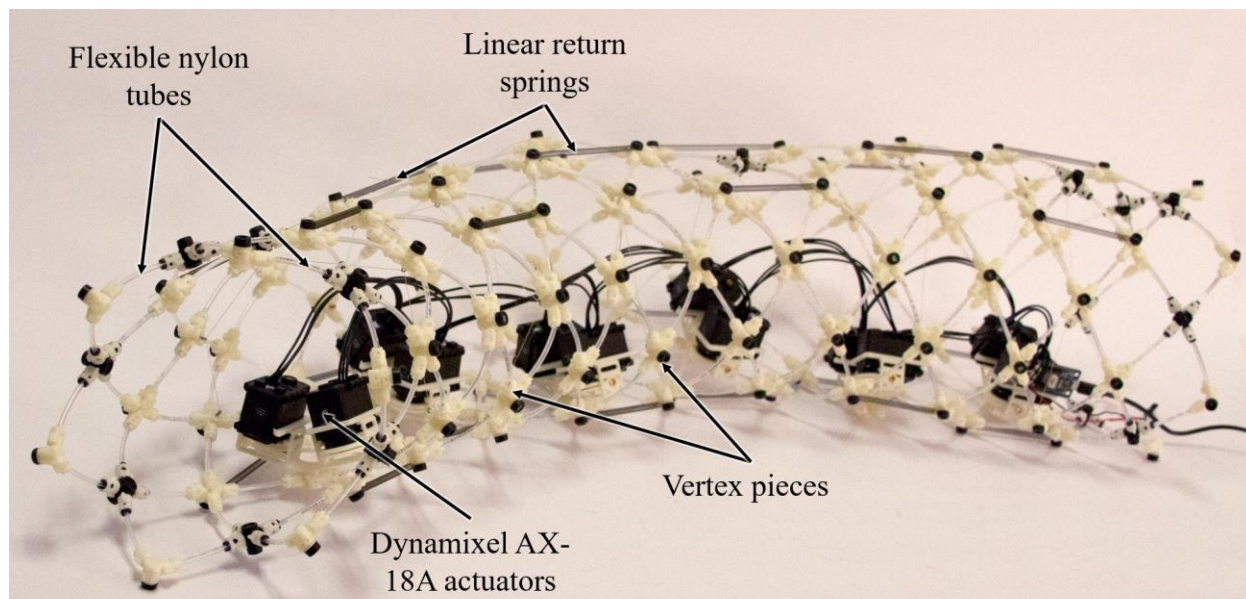

Figure 1: Compliant Modular Mesh Worm-Steering (CMMWorm-S) in an arc-like configuration. Each segment includes two actuators that allow bending for turning. The various components of the robot mesh are labelled.

The basic configuration and circumference of CMMWorm-S are similar to our previous worm-like robot CMMWorm-O, a cable actuated, multi-segmented soft robot (Horchler et al 2015b). In CMMWorm-O each segment was actuated by a single servomotor so that different segments of the robot can achieve different diameters, smoothly deforming the mesh body. CMMWorm-O's mesh is comprised of short "links" of flexible tubing or rod, secured by quick-connect air hose fittings that were embedded in rigid vertex pieces. The vertex pieces were 3-D printed and their role is to join sections of tubing or rod to prevent relative translation, but allowed relative rotation and permitted attachment and routing of the actuating cables. A motor driven circumferential cable, like the circumferential muscle of the earthworm's segment, was used to contract the segment's diameter. Linear springs along the length of the segment passively returned the segment to its initial maximum diameter state on the removal of the actuation load. CMMWorm-S improves on the design of its predecessor in terms of locomotion capabilities, mechanical robustness, and reduced mass.

The addition of more actuated degrees of freedom allows volitional turning. Each segment of CMMWorm-S is actuated by two smaller Robotis Dynamixel AX-18A servomotors. These actuators are 50% faster as compared to the MX-64T actuators used in the CMMWorm-O robot (97 rpm at 12V as opposed to 63 rpm at 12V), allowing the robot to move faster. Each actuator controls one-half of a segment, i.e. three rhombuses, whereas in CMMWorm-O each actuator controls a whole ring of six rhombuses around the diameter of a segment. The mesh deforms circumferentially according to the amount of cable spooled in by the actuator.
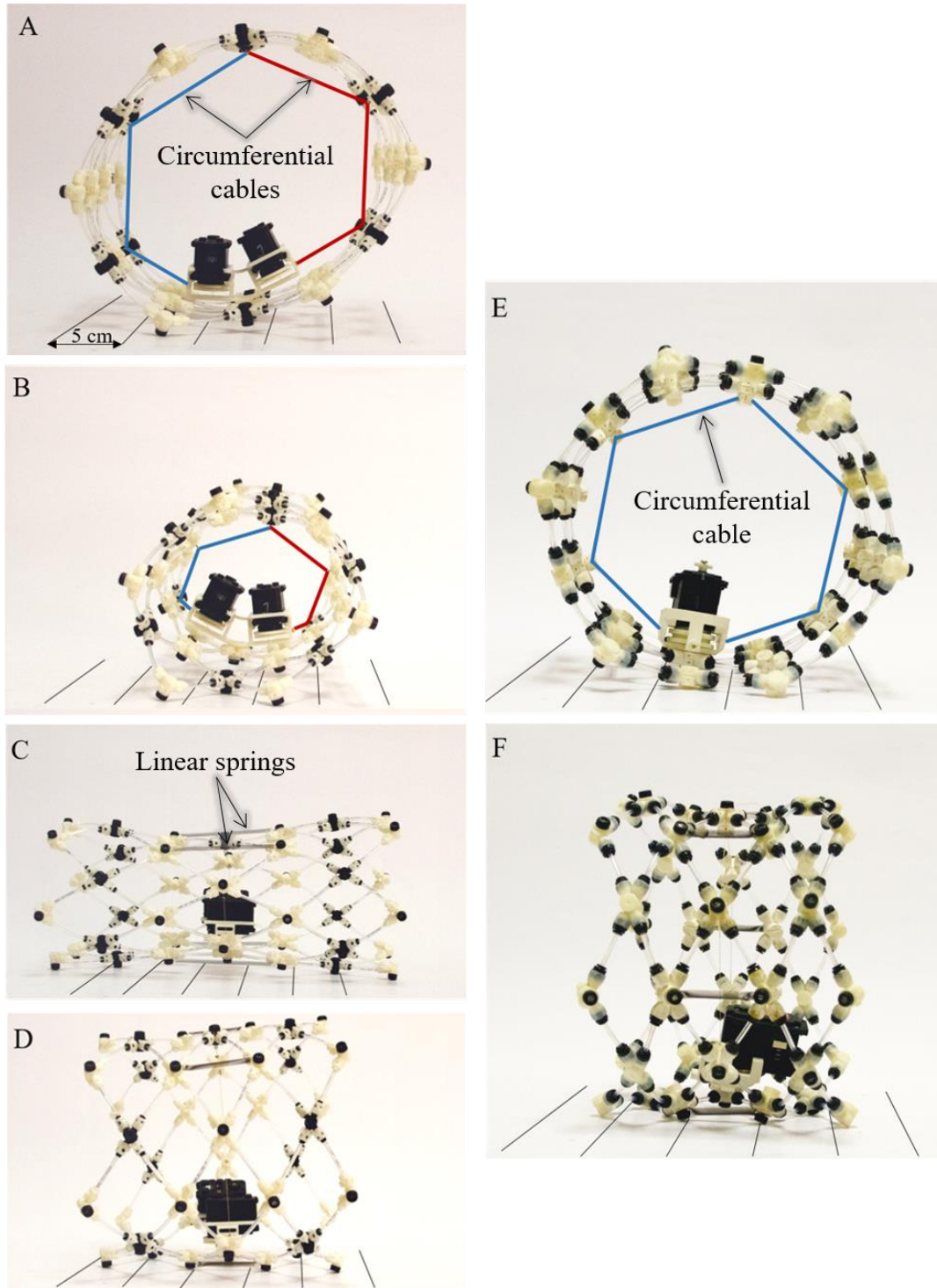
Figure 2: A single segment of the CMMWorm-S (A-D) indicating the segment contraction-expansion cycle and CMMWorm-O (E-F). (A) The two circumferential cables highlighted in blue and red actuated by two different servomotors when spooled equally, allows the segment to contract in diameter (B) while extending in length (C). Springs along the length of the segment return the segment to its maximum diameter as shown in D as the cable is spooled out. (E) A single actuator in CMMWorm-O controls a single cable and hence does not permit differential spooling of cables. (F) Expanded side view of CMMWorm-O.

For straight locomotion, both segment motors operate equally and evenly extend both halves of a segment, increasing the length symmetrically. This extension of each segment during one cycle of a peristaltic wave is defined as the stroke length. To cause the robot to turn, actuators of a segment spool in different cable lengths, thereby causing a segment to extend non-uniformly. This concept was demonstrated in Softworm (Boxerbaum et al 2012) where the tension in the cables was *passively* biased along the length of the robot. In CMMWorm-S, the segment half opposite to the direction of the turn extends more in order to cover a larger distance. For example, if the robot has to turn left, the right side of the robot needs to cover a larger distance as compared to the left side. This difference in the amount of cable spooled in can be achieved in two ways: one side may contract for a longer time period, while keeping the speed of both actuators constant, or the speed of actuation may be different between the two actuators while keeping the duration of actuation constant.
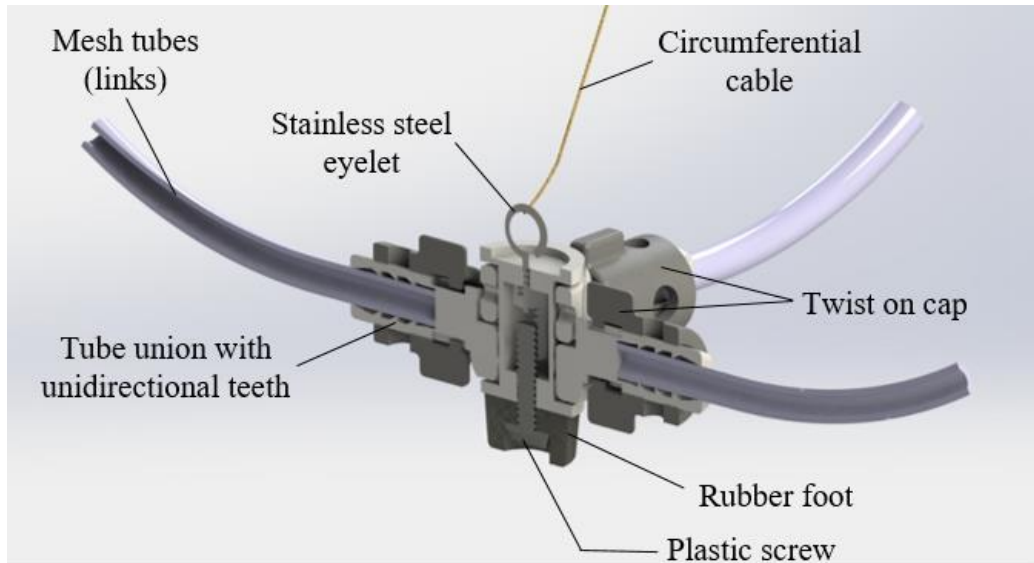

Figure 3: The mesh of the CMMWorm-S is composed of vertex pieces that allow easy connection of tubes. The vertex piece is composed of the tube union that firmly holds the tubes in place, the twist on cap that clasps the tubes down inside the tube union, a stainless steel eyelet for the passage of the actuation cable and a rubber foot that helps in traction during locomotion. The tube union and twist on caps are 3-D printed separately in acrylonitrile butadiene styrene on a Stratasys Fortus 400mc FDM (fused deposition modeling) machine with 0.245 mm (0.010") slice height ±0.127 mm (0.005") tolerance. The vertexes permit rotation about the axis through the screw.

The improved modular design of CMMWorm-S gives us the opportunity to exchange components and test for different and softer stiffness properties. The new design incorporates smaller vertex pieces without push-in Legris™ fittings. The quick connect Legris fittings used on CMMWorm-O were expensive, bulky and had to be machined and epoxied into the vertex pieces. The size and rigidity of the vertex pieces is a limiting factor in reducing the stiffness of the robot. In CMMWorm-O, high stiffness springs and stiff mesh tubes had to be used to maintain maximum diameter and a uniform shape due to bulky vertex pieces. The new design of the vertex pieces (figure 3) incorporates unidirectional teeth inside the tube union, and a twist on cap to clasp the tubes inside the vertex pieces. This design change replaces the Legris fittings and ensures that the tubes do not slip out during motion of the robot. Due to the smaller size of the vertex pieces, the robot can incorporate softer tubes and softer linear springs, thereby decreasing the overall stiffness of the robot.

In CMMWorm-O, the actuation cable passed through slots in the vertex pieces causing a large amount of friction acting on the cables. This lead to cable wear and frequent breakdowns. The cables in CMMWorm-S pass through stainless steel eyelets threaded into the vertex pieces. Eyelets have helped in reducing friction, thereby reducing uneven deformation and frequent cable breakage.

These design changes were necessary to conduct the research presented in this paper. CMMWorm-S is able to locomote forward and turn via peristalsis and its components can be easily exchanged and its stiffness can be reduced as compared to CMMWorm-O. Furthermore, the mass of the new robot is 37% less than CMMWorm-O. These improvements allowed us to perform empirical studies into the relationships between component, segment and body stiffness versus forward and turning locomotion.

3. Electronics and Control

CMMWorm-S is actuated by twelve Dynamixel AX-18A servomotors that incorporate sensors for feedback control. These actuators are connected through a serial bus. In order to reduce voltage drop, the actuators are connected in two parallel chains comprising six actuators on each side. Each chain of actuators is connected to a microcontroller, which is powered by an off-board DC power supply. The AX-18A actuators have a 300° encoder along with position, speed, and load feedback capabilities. The actuators' sensory capabilities allow data logging without the need for additional sensors on the robot (Kandhari et al. 2016).

A single Robotis OpenCM9.04 microcontroller (32-bit ARM cortex-M3, STM32F103CB, 72MHz) is used for control. The microcontroller is mounted on the side of an actuator at the end of the robot. It communicates with the AX-18A actuators at 1MBps. Programming of the microcontroller and data logging are performed over a USB to PC connection.

Our open source DynamixelQ library (Horchler 2015a) for the Open CM9.04 microcontroller enables high-speed communication with AX and MX series Dynamixel actuators. The library has syntax that allows reading and writing to multiple actuators simultaneously.

A time-based control scheme generates waves along the length of the robot to produce locomotion. For all the tests performed throughout this article a 3×1 wave (where 3 represents the number of segments per wave, including suspended segments, and 1 the number of waves along the body) was used (Horchler et al 2015c). The 3×1 wave has two pairs of segments working in conjunction, as one segment expands in diameter, the other contracts. Between both active segments is a contracted inactive (suspended) segment referred to as the spacer segment. Thus, at any given time, four actuators are active within CMMWorm-S. The actuators are configured to speed-control mode and are simultaneously commanded to move at a specified speed, with maximum torque for a fixed duration. The next set of actuators in the wave sequence are activated immediately after the previous duration terminates. For straight-line locomotion, all four actuators are controlled at the same speed. In contrast, for turning, the actuators controlling the side opposite of the direction of the turn are controlled at speeds greater than the actuators on the inner side for the same duration. The difference between the speeds of these actuators is referred to as the bias. This allows the outer side to extend by a greater distance as compared to the inner side. All the turning experiments were carried out with a 75% bias, i.e. the rpm of the inner actuator were 75% slower than the outer actuator.

$$\text{Bias} = \frac{\text{Outer actuator speed} - \text{Inner actuator speed}}{\text{Outer actuator speed}} \tag{1}$$
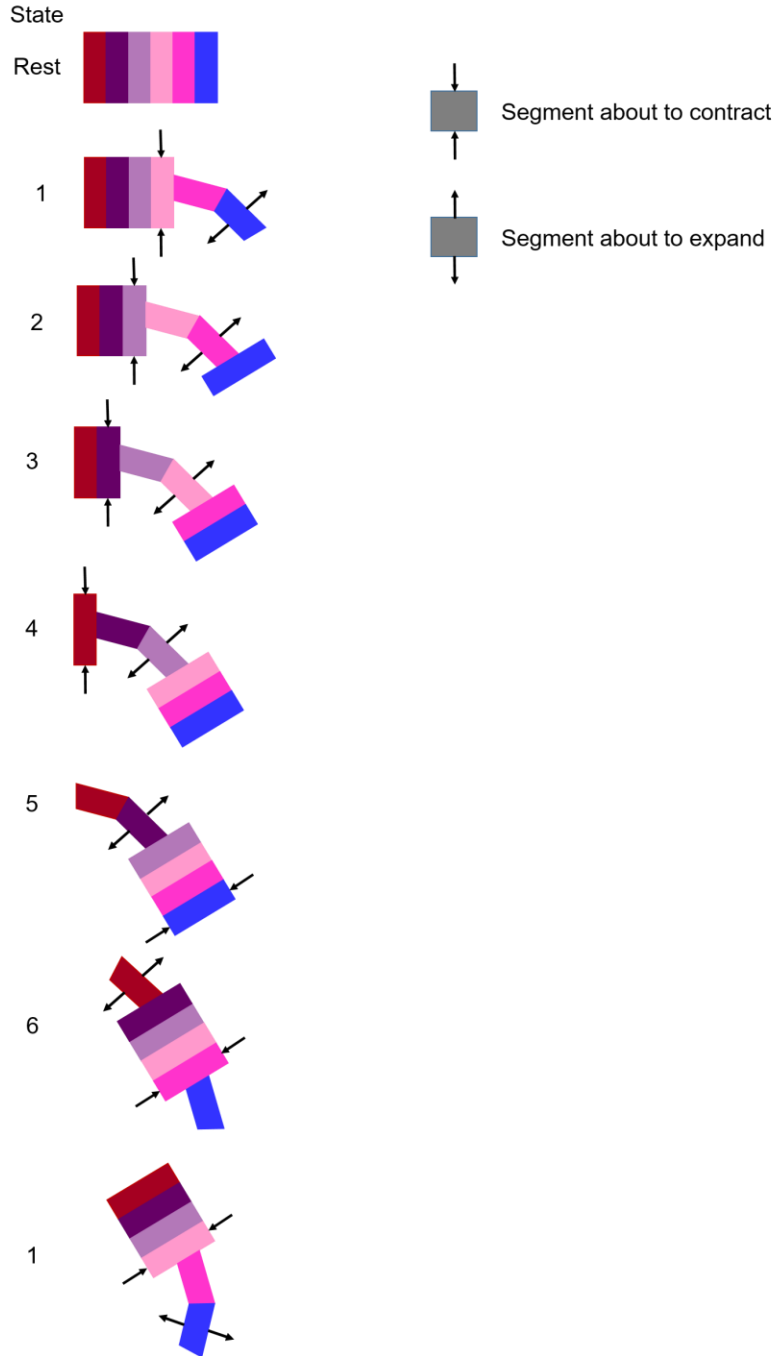
Figure 4: Turning mechanism schematic as seen from the transverse view, as the cables are spooled in with a uniform bias, the segment contraction is uneven causing each segment to expand unevenly. The outer side contracts more than the inner side and that causes the robot to turn. Between a contracting and expanding segment is an inactive contracted segment referred to as the "spaces segment". Note: due to friction and slip, the robot does not turn by such large angles as shown in the schematic.

4. Methods and Results

We empirically characterized the properties and performance of the robot using components of different stiffness. Three types of flexible tubes of varying internal diameter and material (table 1) are used to vary the mesh-tube stiffness. The other compliant components of the mesh are the springs that help return the

segment to its expanded state after the actuation load has been removed. Two different springs were used with stiffness values of 0.45 N/cm and 1 N/cm. The springs are attached along the length of the segment between rhombuses. Springs of equal stiffnesses are attached on both sides such that the stiffness properties on either side of a segment are uniform. Figure 5 defines the different configurations of springs used in order to obtain different return forces on the segment.

Table 1: Properties of the three mesh-tubes used for testing purposes. The tubes are made of nylon plastic and have varying cross-sectional areas. The bending stiffness was experimentally measured by cantilevering a short length of the tube and hanging a mass at the free end. The flexural rigidity was calculated using the formula: $EI=FL^3/3\delta$, where E is the Elastic Modulus, I is the area moment of inertia, L is the length of the tube and δ is the deflection from the horizontal axis. Type H refers to the tube with the highest bending stiffness, type M for intermediate bending stiffness and type L for lowest bending stiffness. (ID: Inner diameter, OD: Outer diameter).

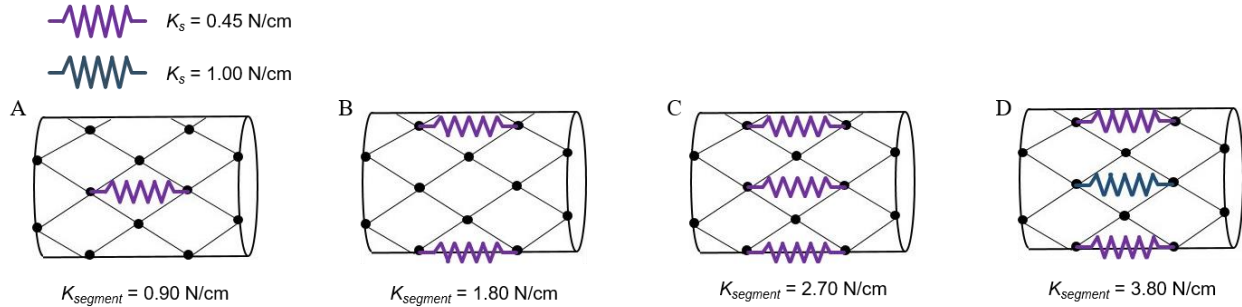| Tube	ID (Do) (mm)	OD (Di) (mm)	Bending Stiffness ($EI/3L^3$) (N/cm)
Type H:	1.85	3.175	0.10
Type M:	2.00	3.175	0.03
Type L:	2.36	3.175	0.01

Figure 5: Diagrams showing a segment with different configurations of return springs used in testing. Springs are coil extension spring with stiffness 0.45N/cm and 1N/cm that are attached along the length of the segment, providing a return force after the actuation load is removed. The springs are symmetrically attached around the segment (A) 2×0.45N/cm, (B) 4×0.45N/cm, (C) 6×0.45N/cm and (D) 4×0.45+2×1 N/cm.

4.1 Characterization of Stiffness

Characterization of stiffness of an individual rhombus:

To better understand the kinematics and the softness of our mesh-based robot, we first extracted a single rhombus with a return spring and subjected it to a longitudinal force while measuring the change in length (figure 6). The rhombus is composed of four vertex pieces connected via tubes or "links" and a linear spring attached along the diagonal of the rhombus, providing a force to return the rhombus to its initial rest state. In a completely rigid mechanism, the rhombus would extend until the included angle between the vertex

pieces reached its maximum limits (rigid contact between components of the vertices). However, in the case of a rhombus with flexible tubing, it can bend further: it is capable of bending until an upper limit is reached (maximum bending of links as shown in figure 6: see appendix A). This test was used to quantify the effect that flexible tubes have on the stiffness of an individual rhombus.
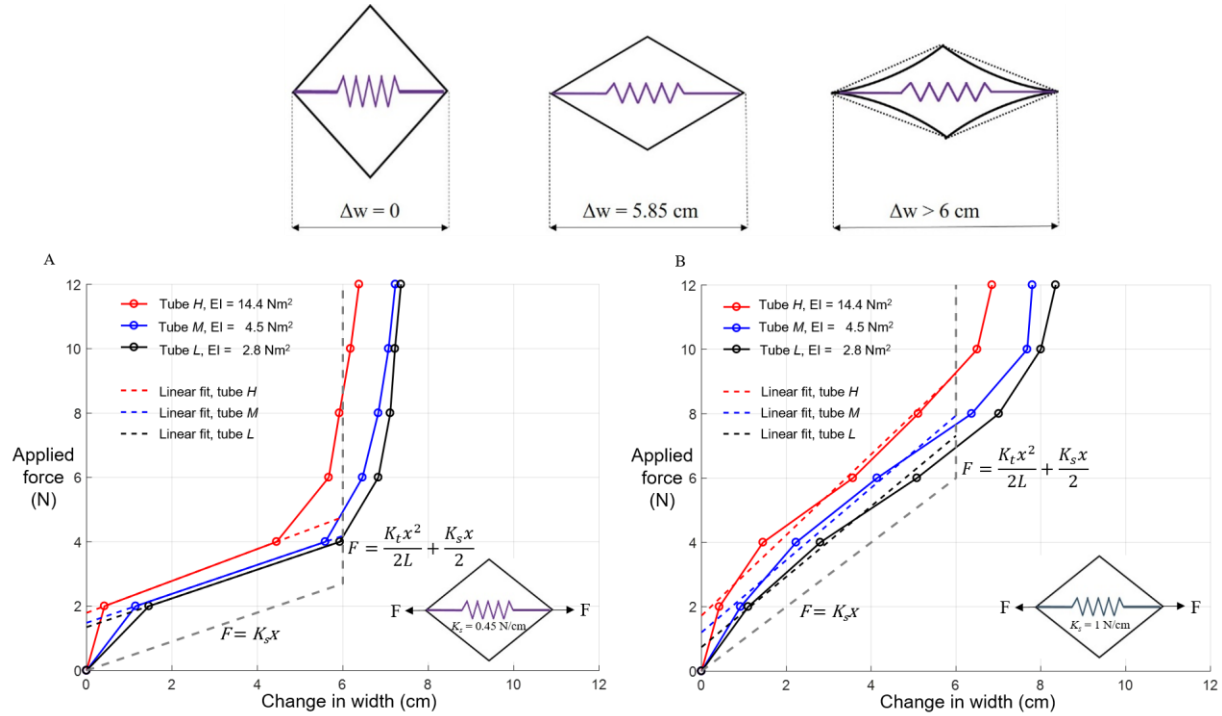

Figure 6. Change in width (Δw) of a rhombus as a force is applied along the diagonal of an isolated rhombus in a planar setting for three tube types and two springs (0.45N/cm for A and 1N/cm for B). The total change in width without tube deformation is 5.85 cm. Beyond that, the tubes start to bend inwards, deforming the rhombus as shown. The total change in width up to 5.85 cm is expected to be linear and due to the return force of the spring only. Beyond this, the bending and longitudinal stiffness of the tubes cause the force to increase with a sharp change in slope of the curve (stiffness). Each tube then acts like a spring, with spring stiffness K_t. The stiffness of tube type *L* is the least, so that maximum deformation is observed. Tube deformation decreases with an increase in tube stiffness as seen in both A and B. A linear fit up to 6 cm (linear working zone) is used to find the stiffness of the rhombus with different components.

Based on the kinematic constraints of the vertices, the total extension possible without bending the tubes is approximately 6 cm. Beyond that, the tubes are loaded in tension and in bending moment. Thus, they start to bend and the rhombus stiffens but not infinitely as would be the case if the tubes were rigid.

This characterization of the stiffness of an individual rhombus leads to the conclusion that the spring stiffness is the main factor determining the stiffness of the rhombus in the longitudinal direction in the robot's normal operating range (table 2). Beyond this, links are in tension and bending as shown in Fig 4, increasing the rhombus width, even though the vertex pieces have reached their maximum included angle limits.

Table 2: Rhombus stiffness measured from the slope of the linear fit as shown in figure 6. Measured rhombus stiffness is compared to the stiffness of the individual spring for different tube types, showing the contribution of the tubes towards the stiffness of an individual rhombus. Measured rhombus stiffness is

similar to the stiffness of the spring for the case of Figure 6A but as the spring stiffness increases, the tubes add to the overall rhombus stiffness (Figure 6B).

Tube	Spring Stiffness (N/cm)	Calculated Stiffness (N/cm)
Type H	0.45	0.49
	1.00	1.25
Type M	0.45	0.45
	1.00	1.12
Type L	0.45	0.45
	1.00	1.09

Characterization of stiffness of a segment

The results from individual rhombus stiffness help in predicting the stiffness of a segment of the robot. The segment is radially symmetric and has three stiffness components: (a) longitudinal stiffness due to tensile forces applied along the length of the segment, (b) circumferential stiffness due to compressive forces applied perpendicular to the length of the segment and (c) bending stiffness due to different diameters between adjacent segments (straight-line locomotion) or within the same segment (turning).

We measured the contribution of each component of the mesh to the stiffness of a segment. To do so, an isolated segment was subjected to forces in both longitudinal and circumferential directions, while measuring the changes in longitudinal length and circumferential height, respectively. To measure the bending stiffness, the deflection of a vertically loaded cantilevered segment was measured from a horizontal line.

Longitudinal Stiffness

We measured the longitudinal stiffness of a segment constructed with tubes of differing stiffnesses (figure 5). A segment is composed of six rhombuses connected in a ring-like pattern. When subjected to a tensile force along its length, the segment extends in length while contracting in diameter (similar to hydrostatic coupling observed in earthworms). A tensile force up to 12N was applied in increments of 2N, and the change in segment length was measured. The resultant plot allows calculation of the stiffness (slope of the curve) of a segment along its longitudinal axis and comparison of the result to a stiffness calculated from the expected rhombus stiffness (longitudinal return springs connected in parallel = K_s, see Table 2).
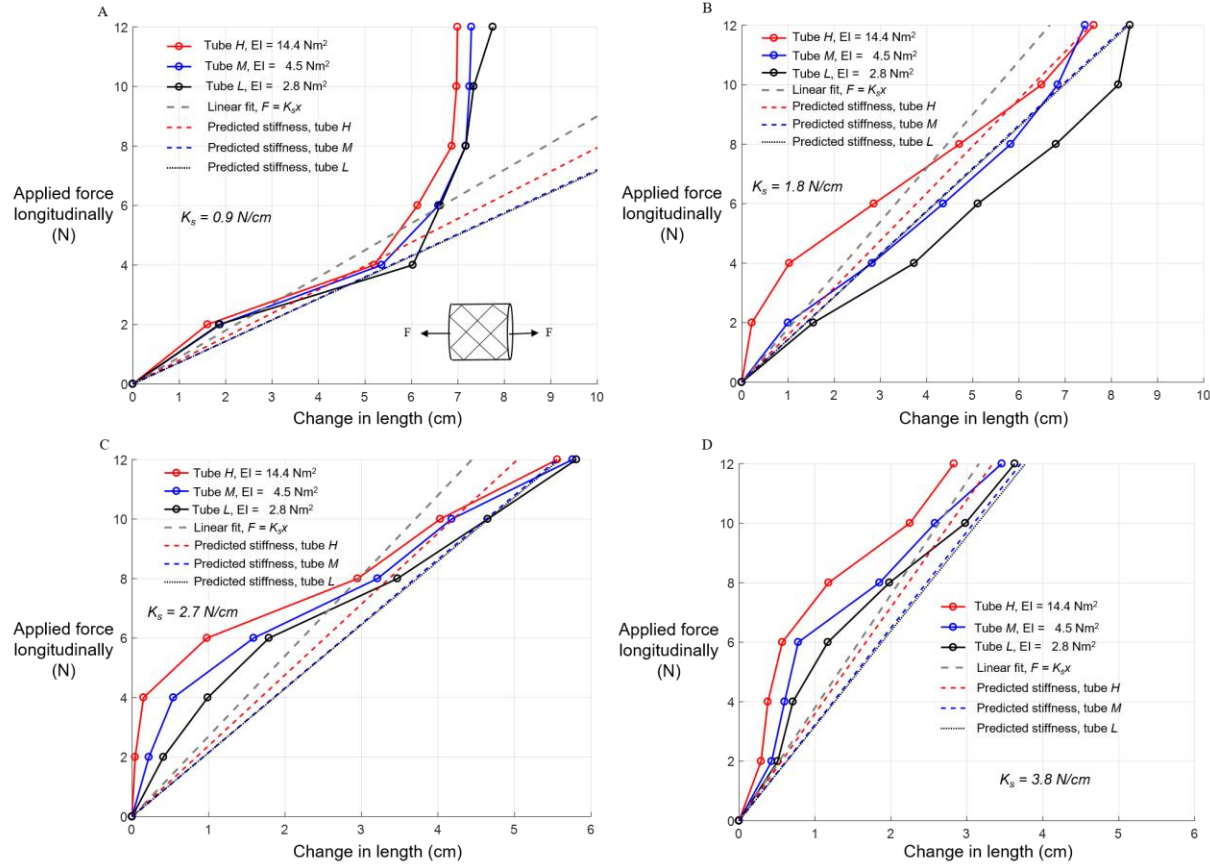
Figure 7: Change in length of an isolated segment as a tensile force was applied for four different spring stiffness configurations (figure 5). The colored dashed lines are the predicted stiffness of the segment based on the calculated rhombus stiffness (table 2). The slope of the gray dashed line is the equivalent stiffness of the return springs attached in the segment, i.e. K_s, the sum of the stiffnesses of each of the longitudinal return springs in that segment for the four different configurations shown in Figure 5. Red, blue and black solid lines join the experimentally measured points. The region of the curve up to an extension of 6 cm is used to estimate the longitudinal stiffness of the segment. In case of configuration D (K_s = 3.8 N/cm, maximum extension = 3.6 cm), the entire curve is used to estimate the stiffness of the segment. Note that in the first configuration, predicted and actual values are very similar but for the other configurations the predicted values are less accurate.

As observed in the case of a rhombus, the main factor determining a segment's longitudinal stiffness is the sum of the segment's longitudinal return springs (K_s, see figure 8). Increasing the stiffness of the return springs increases the longitudinal stiffness of the segment. In addition, similar to the case of the rhombus, links with higher bending stiffness resulted in higher segment stiffness. However, the measured stiffness of the segment is lower than the predicted stiffness; this difference is due to the links bending out of plane when connected in a ring-like pattern.
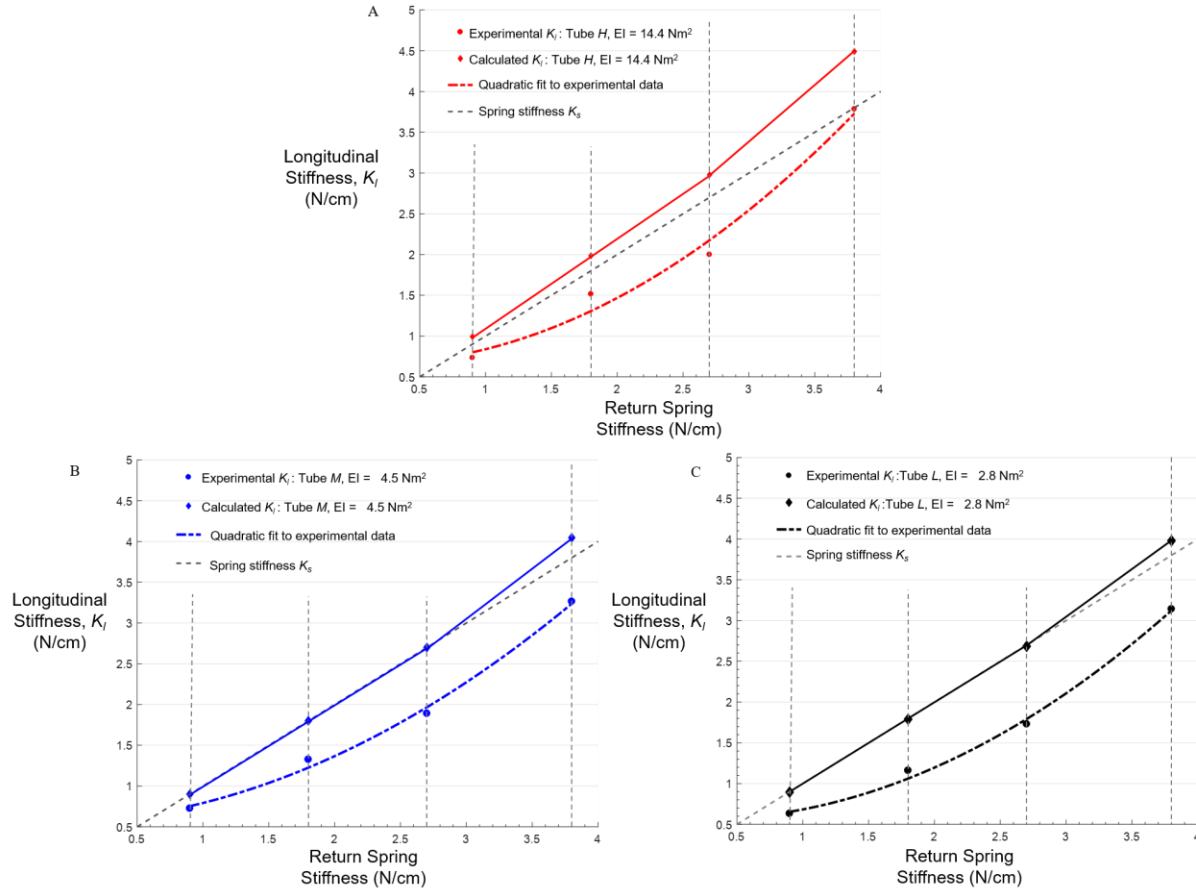
Figure 8: Longitudinal segment stiffness for each configuration as measured from Fig. 7 compared to the predicted stiffness (solid lines) from the rhombus model and the stiffness of the return springs (gray dashed line). The measured longitudinal stiffness is less than the predicted stiffness for each tube type from the rhombus model due to the bending of the links when connected in a ring-like structure. The measured longitudinal stiffness is thus a function of both tube bending stiffness and return spring stiffness. The colored dashed line indicates a quadratic fit for each tube type. The return springs have a major contribution towards the longitudinal stiffness, as there is a noticeable difference between the longitudinal stiffness of different configurations (vertical dashed lines). The difference in stiffness values for different tubes for the same configuration is very small compared to different spring configurations (figure 5). The predicted value for tube types M and L overlay the spring stiffness line up to 2.7 N/cm.

Circumferential Stiffness

Appropriate circumferential stiffness is also important for peristaltic locomotion of a worm robot. If the robot were too compliant, then on actuation, the mesh would deform unevenly causing locomotion to be less efficient. On the other hand, if it is too stiff, the motors could not deform it within and between segments and the robot could not move. Therefore, an efficient robot must strike a balance between these extreme limits. The structure must be compliant enough to bend and deform evenly while being able to maintain structural integrity. We measured circumferential stiffness by applying a compressive force normal to the length of the robot.
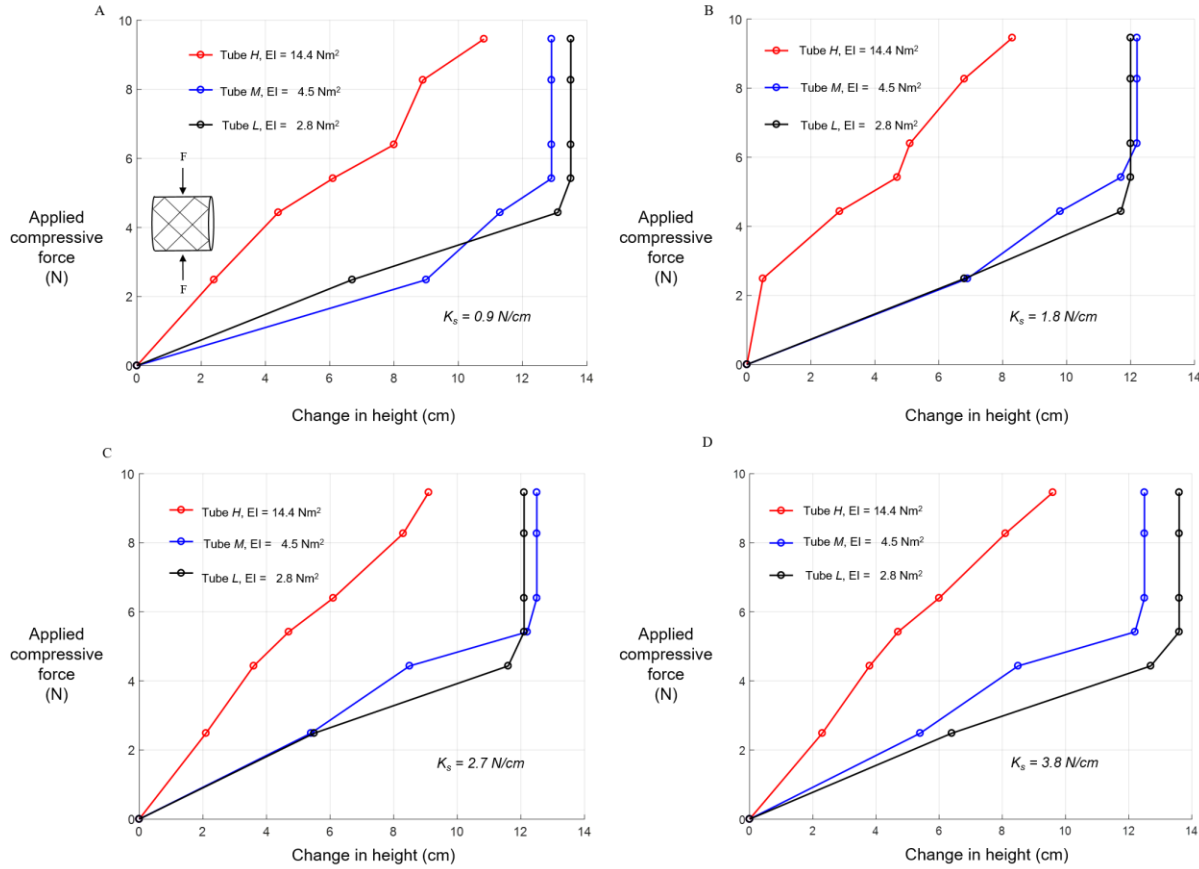
Figure 9: Change in height of an isolated segment when a compressive force was applied radially for different longitudinal spring configurations (figure 5). The maximum compression in height is approximately 13 cm, where the top of the segment is in contact with the actuators. The curve becomes vertical at approximately 13 cm as further deformation is not possible. A linear fit to the curve from 0 cm to 13 cm was used to estimate the circumferential stiffness of a segment. For tube types M and L, maximum deflection is observed with the application of a minimum of approximately 4.5 N (all configurations), while for tube type H, maximum deflection is not attained with applied load as large as 9.5 N.

The circumferential compressive stiffness of the segment is dependent on the stiffness of the links more than it is on the stiffness of the return springs (figure 9). When a compressive force is applied on the segment, tubes with larger bending stiffness resist deflection to a greater extent. Tubes with lower bending stiffness comply with the load more easily. There is a noticeable difference between the segment's circumferential stiffness for tube type H, the stiffest tube, as compared to segments with the other tubes (figure 10).

There is an upper limit to the circumferential stiffness of a segment as the return spring stiffness increases (figure 10). Beyond that limit, if the return spring stiffness is increased, the segment cannot maintain the height-width coupling. The links are unable to transfer the decrease in height to an increase in length. Instead, the segment undergoes the phenomenon of "barreling" due to compressive loads. The cross-sectional shape of the segment changes from circular to oval. The higher the tube stiffness, the more resistant the segment is to barreling. Thus, a down-facing parabolic function was observed in the plot of circumferential vs. return spring stiffness as K_s was increased.
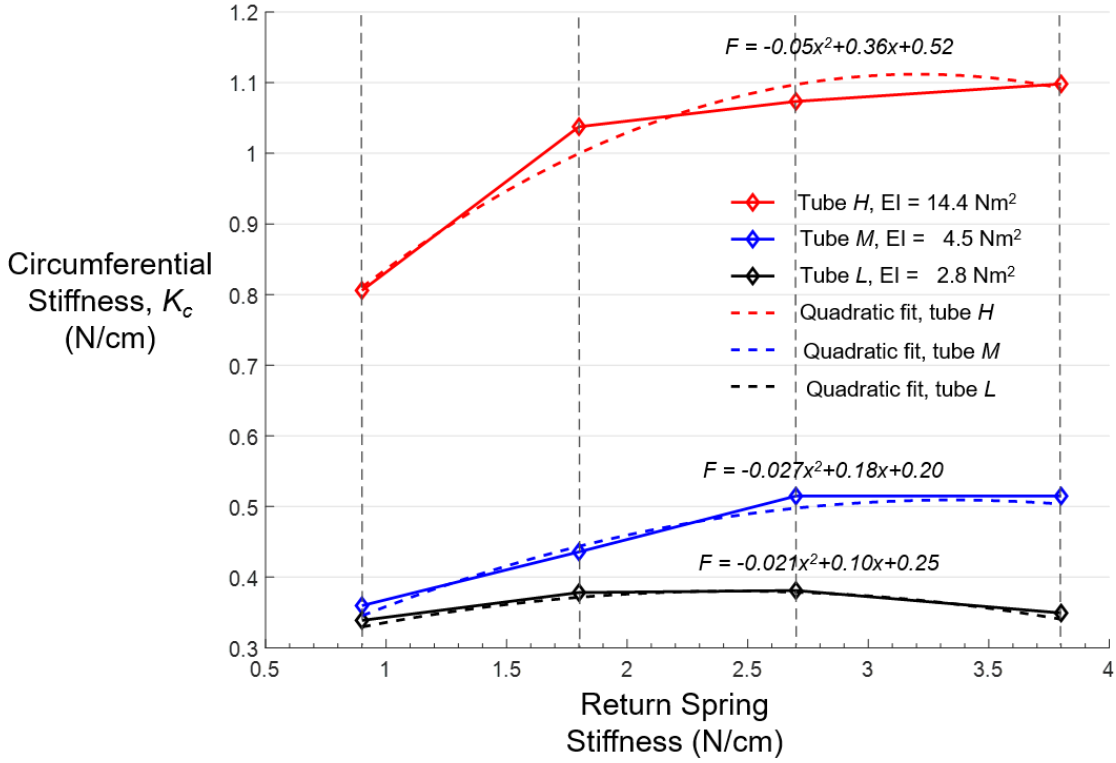
Figure 10: Circumferential stiffness as measured from Fig. 9 shows a non-linear relationship between circumferential stiffness and return spring stiffness. A downward parabolic curve (quadratic fit) was observed as the spring stiffness increased in each case. There is a noticeable difference between the circumferential stiffness of tube type H and the others due to its larger bending stiffness. However, the difference between the other tube types is small.

Bending Stiffness

The worm robot body's bending stiffness is also important for its performance. During peristaltic locomotion, adjacent segments achieve different diameters. Bending stiffness provides a measure of the ability of a contracted segment to support itself between expanded anchoring segments. Thus, bending stiffness can reduce frictional drag.

Bending stiffness of the robot is measured by cantilevering segments. Multiple segments of the six segment robot are supported on a table and one or two segments are cantilevered at the end of the table. The cantilevered segments bend due to their own weight, which is assumed to be evenly distributed along their length. The deflection along the length allows us to calculate the Young's or elastic modulus (E) and the bending stiffness of the robot. Young's modulus is measured using the equation:

$$E = \frac{WL^4}{8\delta I} \tag{2}$$

where W is the distributed load per unit length, L is length, δ is deflection from the horizontal axis and I is the area moment of inertia.

As can be seen in figure 11, the elastic modulus depends on the tube-link bending stiffness and the return spring stiffness. The elastic modulus of a segment increases with increasing link bending stiffness and more so with greater return spring stiffness. The elastic modulus also increases with return spring stiffness. However, beyond a maximum, for softer tubes M and L, increasing the return spring stiffness causes the bending stiffness to decrease. As the tube stiffness increases, the resistance to uneven deformation increases. However, on further increasing spring stiffness, the tubes can no longer resist the force and start to bend and contort non-uniformly. The tubes kink or bend out of plane such that the return springs undergo minimum elongation. Thus, both return springs and link stiffness affect a segment's bending stiffness. Interestingly, although the robot includes some relatively rigid components, its elastic modulus is in the range of soft materials.

Summary of Stiffness Properties

Table 3 summarizes segment longitudinal, circumferential and bending stiffness for different tube and return spring stiffness values and configurations. The link stiffness strongly affects the circumferential stiffness, whereas return spring stiffness most strongly affects longitudinal stiffness. The bending stiffness follows a similar pattern to that of the circumferential stiffness. Greater link bending stiffness results in greater bending and circumferential stiffness of the segment; beyond a maximum value, increasing the return spring stiffness causes the bending stiffness to decrease.
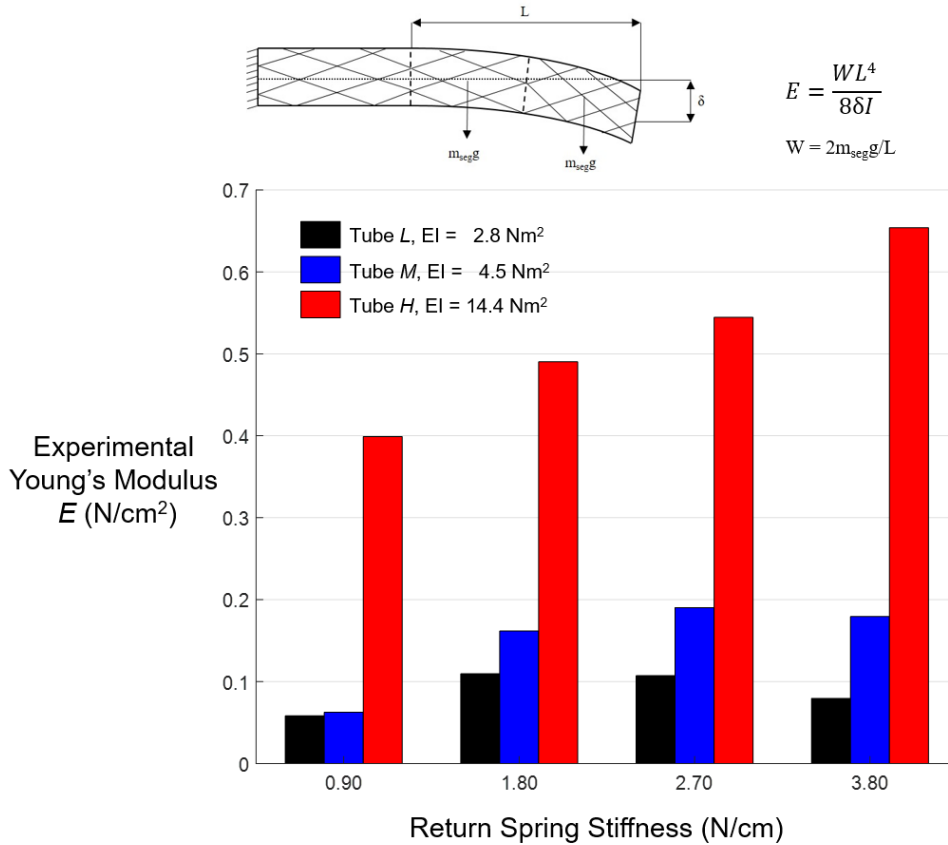

Figure 11: Experimental Young's modulus measured for the six-segmented CMMWorm-S. Young's modulus is measured using the equation $E=WL^4/(8\delta I)$, where W is the distributed load per unit length, L is length, δ is deflection from the horizontal axis and I is the area moment of inertia. Although composed of relatively rigid components, Young's modulus of our robot lies in the range comparable to soft material.

Table 3: Summary of segment stiffness properties for different configurations.

Tube	Return Spring Stiffness (K_s) (N/cm)	Longitudinal Stiffness (K_l) (N/cm)	Circumferential Stiffness(K_c) (N/cm)	Bending Stiffness ($K_b = EI/L^3$) (N/cm)
Type H	0.90	0.73	0.80	2.36
	1.80	1.51	1.03	2.43
	2.70	1.99	1.07	3.10
	3.80	3.78	1.09	3.87
Type M	0.90	0.72	0.35	0.32
	1.80	1.32	0.43	0.76
	2.70	1.88	0.51	0.94
	3.80	3.26	0.50	0.89
Type L	0.90	0.63	0.33	0.33
	1.80	1.13	0.37	0.50
	2.70	1.73	0.38	0.50
	3.80	3.14	0.34	0.45

4.2 Robot Locomotion Performance as a Function of Stiffness

With a better understanding of the stiffness properties of the robot from the above studies, we analyzed the performance of the robot as a function of stiffness. Videos from the transverse view were recorded for both straight-line locomotion and turning. All experiments were recorded with the robot crawling on wood (μ_s = 0.85) in order to reduce the effect of slip.

Straight-Line Locomotion

Figure 12 illustrates that the robot achieved greater speed with stiffer tube-links. The robot made increasingly greater forward progress per peristaltic cycle as the tube stiffness was increased from Type L to Type M to Type H tubes. We attribute this speed difference to two observations. First, uneven deformation was observed with less stiff tubes. The stiffer tubes allow better transfer of forces along the rhombus mesh. As the tube stiffness decreases, the tubes closer to the actuator bend easily and do so rather than transferring forces evenly throughout the mesh. Thus, progress per peristaltic wave decreases as the stiffness of the tubes decrease. Another important factor for efficient locomotion is the ability of adjacent fully expanded segments to lift contracted segments as the contracted segments advance. Greater bending stiffness of the tubes allows lifting of contracted segments instead of dragging them. In the case of softer links, both uneven deformation of tubes and the inability of anchoring segments to lift adjacent contracted segments led to poor overall forward progress.
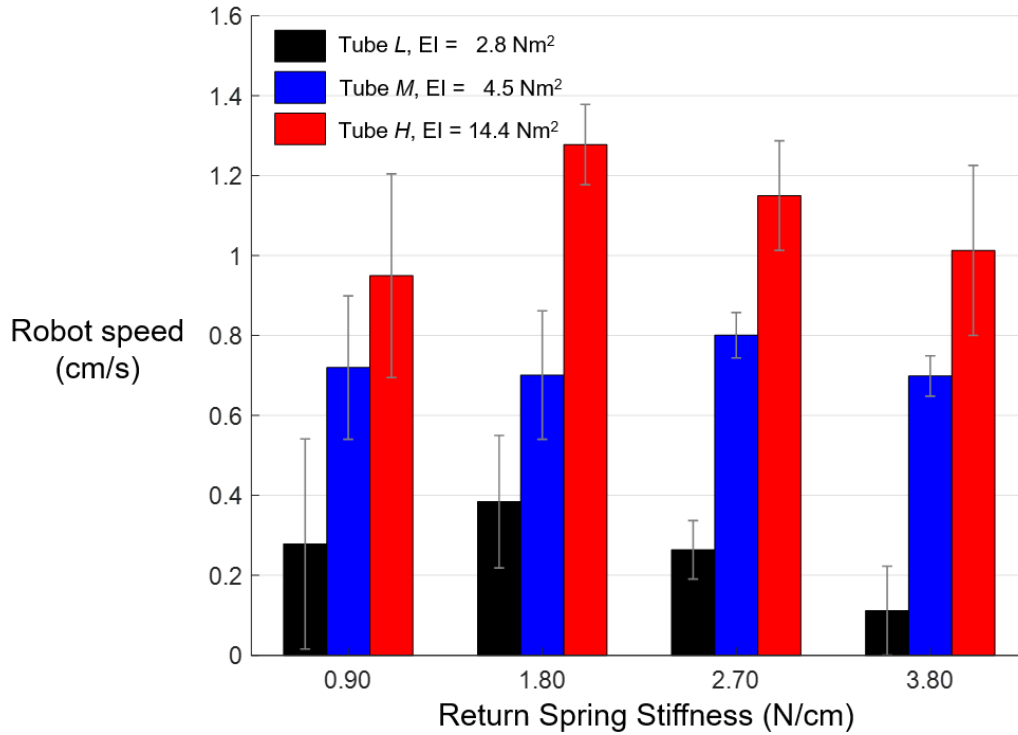
Figure 12: Forward progress per peristaltic cycle (N=12) for each configuration was measured and compared. Forward progress was measured by commanding the actuators to run at zero bias at 70 rpm. A video from the transverse view was taken for each run. Frames were extracted at the end of each cycle and ImageJ (version 1.48, National Institute of Health) was used to measure the progress made per peristaltic cycle. The robot made greater forward progress with stiffer tubes.

A comparison of speed in figure 12 for different segment configurations suggests three trends. First, a larger variation was observed in the first configuration (Figure 5A, K_s = 0.9 N/cm). This is because the return spring force is not sufficient to expand the segment to its original maximum diameter once the actuation load is removed. That is, after extension, the overall robot length elongates and tends to lose efficiency due to the inability of the segments to return to their maximum diameters. Second, as the spring stiffness increases, the actuators require more force to contract a segment to its minimum diameter, and due to the actuators limitations they fail to do so when the return spring stiffness is greater than 1.8 N/cm, thereby decreasing the overall achievable progress (stroke length). Third, forward locomotion strongly depends on the bending stiffness of the links. For all return spring stiffnesses tried, links with higher bending stiffness had better performance. However, while the tubes need to be sufficiently stiff in order to transfer forces and lift adjacent segments, they need to be soft enough to be deformed by the motors and to be connected in a ring-like pattern and deform evenly as the wave travels down the body.

Turning

Experiments were performed to determine the turning performance of the robot (figure 13) in terms of its mean angle turned (figure 14A) and progress made (figure 14B) per peristaltic cycle. The actuators were run at 75% bias (inner actuator speed = 18 rpm, outer actuator speed = 70 rpm). The angle turned was determined by measuring the angle between straight lines drawn from the actuators of the first segment to

the actuators of the last segment before and after each cycle. Progress made while turning was measured by multiplying the angle by which the robot turned and the radius of curvature about a fixed turning point. The product is the arc length, which is defined as the progress made while turning.
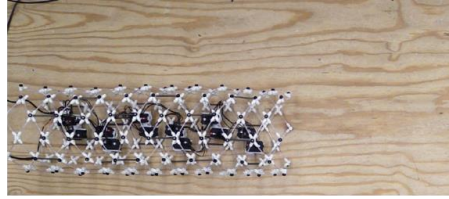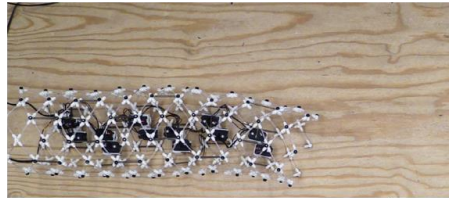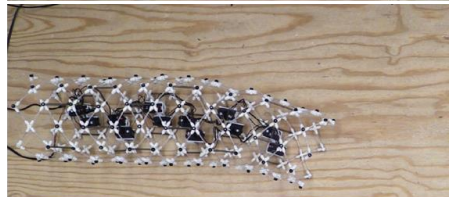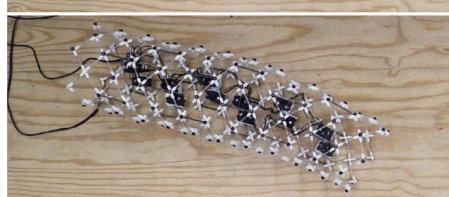

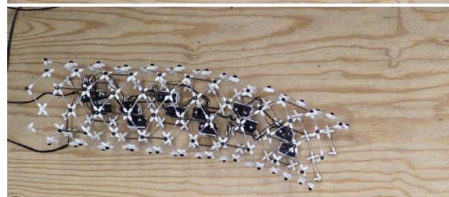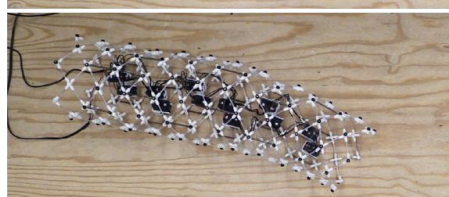**Figure 13:** Video stills of the CMMWorm-S robot turning on a wooden surface. Each still corresponds to the beginning of a new peristaltic cycle.

While turning, the halves of a segment must be capable of achieving different longitudinal elongations. Thus, the segment should be soft enough to achieve different lengths on either side (length bias), while being stiff enough to have a sufficient stroke length. Links with the highest bending stiffness (type H) had maximum angle turned per peristaltic cycle as compared to the other types (figure 14A). Even though segments with the softer tubes were capable of achieving different elongation on their sides, the overall extension was less than for the stiffer tubes.

The angle by which the robot turns follows the same trend as the bending stiffness of the robot (figure 14A). As return spring stiffness increases in the case of stiffer links, higher turning angles are achieved. In the case of links with lower bending stiffness, the angle turned per peristaltic cycle reaches a maximum and starts to decrease with increasing return spring stiffness. The reasoning is the same as for bending stiffness: The ability of the links to resist uneven deformation decreases with increasing return spring stiffness. This causes the links to kink and bend out of plane, thereby decreasing the extension. This decrease in extension causes the robot to turn by smaller angles.

Measuring the robot's progress along an arc while turning allows us to plan a path the robot might take while navigating around obstacles. We want to be able to optimize the robot's path. Thus, we measure the forward progress the robot makes while turning with respect to different stiffness configurations (figure 14B). Similar to straight-line locomotion and turning, performance with tube type H is better compared with types M or L. As the stiffness of the springs is increased, the progress made while turning increases and then decreases beyond a maximum.
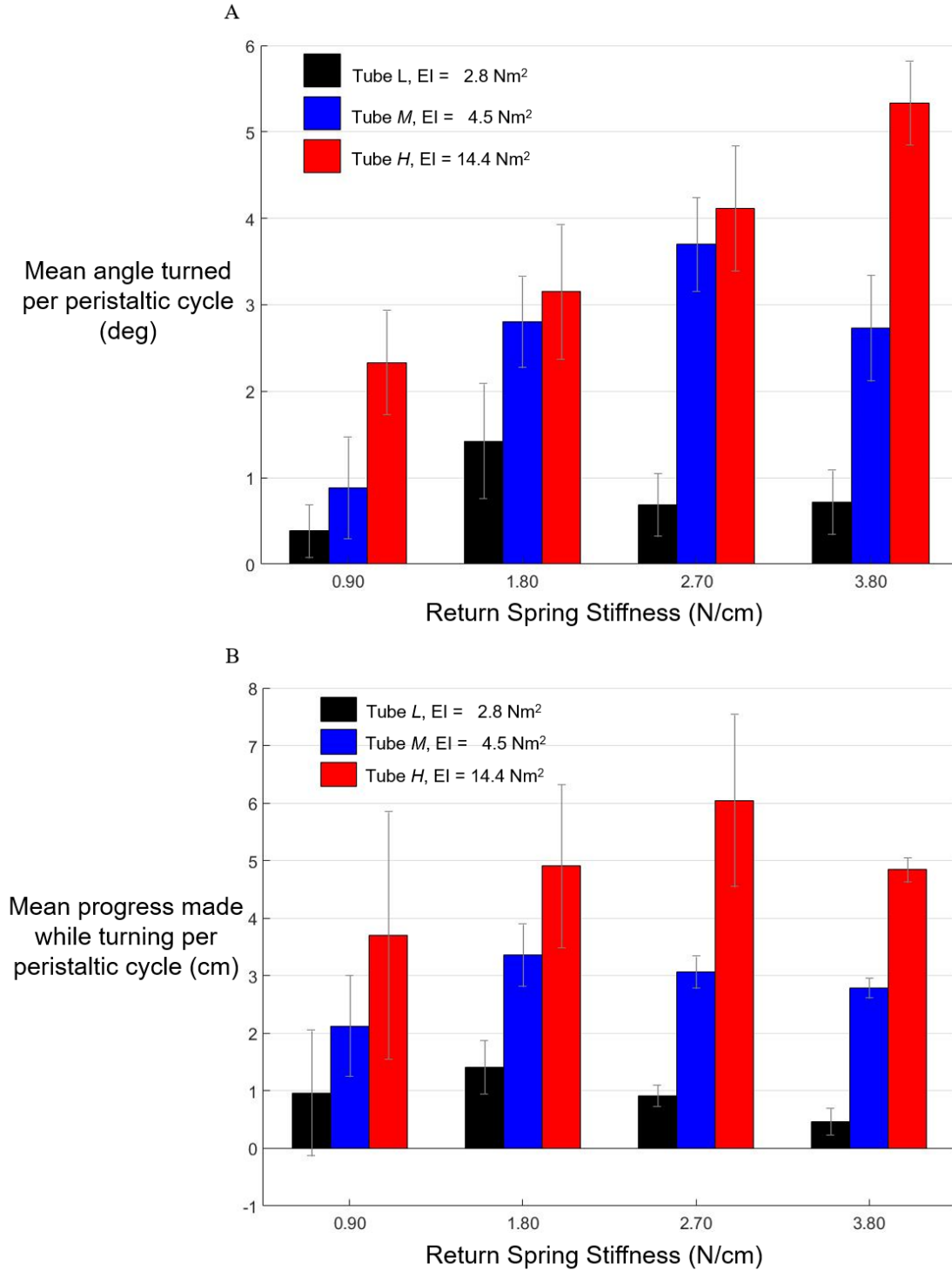
Figure 14: Angle by which the robot turns per peristaltic cycle (N=12) for each configuration was measured and compared. Angle turned was measured by commanding the actuators to run at 75% bias (inner actuator speed = 18 rpm, outer actuator speed = 70 rpm). A video from the transverse view was taken for each run. Frames were extracted at the end of each cycle and ImageJ (version 1.48, National Institute of Health) was used to measure the angle turned per peristaltic cycle. Angle turned was determined by measuring the angle between straight lines drawn from the actuators of the first segment to the actuators of the last segment before and after each cycle. (B) Progress made while turning was

measured by multiplying the angle by which the robot turned and the radius of curvature about a fixed turning point. The product is the arc length, which is defined as the progress made while turning per peristaltic cycle.

5. Conclusions and Future Work

The Compliant Modular Mesh Worm robot with Steering (CMMWorm-S) is a mesh-based robot that uses motor driven cables for actuation. The mesh, composed of 3D printed rigid vertex pieces and flexible tubes, allows interchanging of its components to vary the stiffness of the robot. CMMWorm-S is capable of an entirely new volitional movement, turning, because of the addition of two actuators per segment. Presence of two actuators allows segments to differentially lengthen and shorten, thereby causing turning motion. It is a significant advance over the original robot (CMMWorm-O) that our group had previously developed and described (Horchler et al., 2015). Because the previous robot was only capable of straight-line locomotion, it was not possible for us to study the trade-offs on different behaviors as functions of stiffness of different components. In this paper, we advance in the design and control of a robot capable of multiple behaviors which has not been previously described in the literature. Our results suggest that for CMMWorm-S, increasing circumferential stiffening speeds forward locomotion and increasing its bending stiffness increases its turning angle.

We first examined the effects of tube-link stiffness and return spring stiffness on a single rhombus. For a single rhombus, the resultant stiffness is highly dependent on the return spring stiffness. The longitudinal stiffness of the rhombus is directly proportional to the return spring stiffness, as one would expect from rigid-link mechanism analysis. The tubes connecting the vertex pieces have very little effect on the rhombus stiffness until a limit is reached after which the resultant stiffness greatly increases but not infinitely, as it would with rigid links.

Next, we examined the effects of tube stiffness and return spring stiffness on the longitudinal, circumferential and bending stiffness of an individual segment. Longitudinal stiffness of a segment is strongly dependent on the return spring stiffness. The stiffness along the length of the segment increases as the return spring stiffness increases. Longitudinal stiffness of the segment is, however, less than the predicted equivalent stiffness of rhombuses connected in parallel in a ring-like structure due to the bending of the tubes. An upward parabolic relation is observed for longitudinal stiffness as the return spring stiffness increases. On the other hand, circumferential and bending stiffness of the segment is proportional to the bending stiffness of the links. Increasing the bending stiffness of the links resulted in higher circumferential and bending stiffness. On increasing the return spring stiffness, beyond a maximum, the circumferential and bending stiffness decrease due to uneven deformation of tubes. A downward parabolic relation is observed for both circumferential and bending stiffness. This implies that the return spring stiffness has an optimal based on the structure: It has to be strong enough to return the segment to the original shape but weak relative to the link bending.

We examined the effects of longitudinal, circumferential and bending stiffness of the body on forward locomotion and turning. For our design, the stiffer mesh tubes and return springs resulted in greater forward progress and turning angle per peristaltic cycle. However, in general, fabricating a stiffer robot will not ensure better performance. The ability of the CMMWorm-S to be compliant, and adapt to its surroundings depends on the softness of its tubes. On the other hand, if the tubes are too soft, they undergo uneven deformation and result in inefficient locomotion. This is an important design trade-off.

In straight-line locomotion, circumferential stiffness is most critical. Greater circumferential stiffness leads to greater forward progress per peristaltic cycle (figure 12). Greater circumferential stiffness was achieved

by using links with greater bending stiffness to connect the vertex pieces. Tubes with greater bending stiffness allow more uniform transfer of forces throughout the segment. These tubes also help in maintaining the overall rigidity of the structure during locomotion. However, if the links are too stiff in bending, connecting the rhombuses in a ring-like structure will be difficult. Large bending stiffness of the links will also result in greater coupling between adjacent segments, thus inhibiting neighboring segments from achieving different diameters.

For turning, bending stiffness is most critical. Higher bending stiffness leads to a higher angle turned per peristaltic cycle (figure 14). Bending stiffness is strongly dependent on the bending stiffness of the links similar to circumferential stiffness. However, as the stiffness of the return springs increases, bending stiffness of the robot decreases. Higher bending stiffness helps in achieving a more robust structure. However, if the bending stiffness is too high, it is more difficult to achieve a uniform deformation given actuator strength and structural integrity of the mesh. Bending stiffness should be small enough to allow each side of a segment to achieve different lengths for turning. Nevertheless, if the bending stiffness of the robot is too soft, the segment will be unable to elongate during peristaltic locomotion thus resulting in little forward progress.

To improve overall locomotion with compliant bodies, our work suggests the following design principles. First, reduced robot mass allows for the use of more compliant (less stiff) components. Lighter weight segments allow links with smaller bending stiffness to lift segments and avoid dragging them as the robot advances. Greater segment mass requires stiffer links to allow segments to be lifted. Second, the return springs should not be so stiff that a large amount of actuator force is required to extend the segment and should not be too soft such that the return springs are incapable of returning the segment to its maximum diameter during contraction. In other words, the return spring stiffness should be small enough to allow the segment to undergo maximum extension when acted upon by the actuators and some external resistive force and large enough to return the segment to its maximum diameter rest state.

In order to generalize the above design criteria, we propose a guideline based on the experimental results in this paper. In order to permit the intended soft body deformations for locomotion with a mesh body, the stiffnesses should be related to the body scale as:

$$\frac{mg\Delta L}{\Delta A} < \frac{K_c K_b}{K_l} \qquad (3)$$

where m is segment mass, g is acceleration due to gravity, ΔL is maximum change in segment length for the structure, ΔA is maximum change in segment cross sectional area for the structure (cross sectional area at maximum diameter – cross sectional area at minimum diameter), K_c is circumferential stiffness, K_l is longitudinal stiffness and K_b is the bending stiffness. This single equation expresses that the weight (mg) is supported by the circumferential stiffness (K_c), a large stroke length (ΔL) is permitted by low longitudinal stiffness (K_l), and higher bending stiffness keeps moving segments from dragging on the ground especially if the change in area is small. Thus, the goal is to design a structure to optimize the stiffness ratio ($K_c K_b/K_l$) to permit larger stroke lengths and payloads with less dramatic changes in radius. Our mesh robot accomplishes (3) for every configuration and tube stiffness. However, for the worst performing assemblies, the ratio of the right to left side is about 1. While for the best performing assemblies, the ratio is approximately 30. Beyond this we see a decrease in performance (figure 15, configuration A, tube type H), suggesting there is a maximum limit beyond which performance starts to decrease.
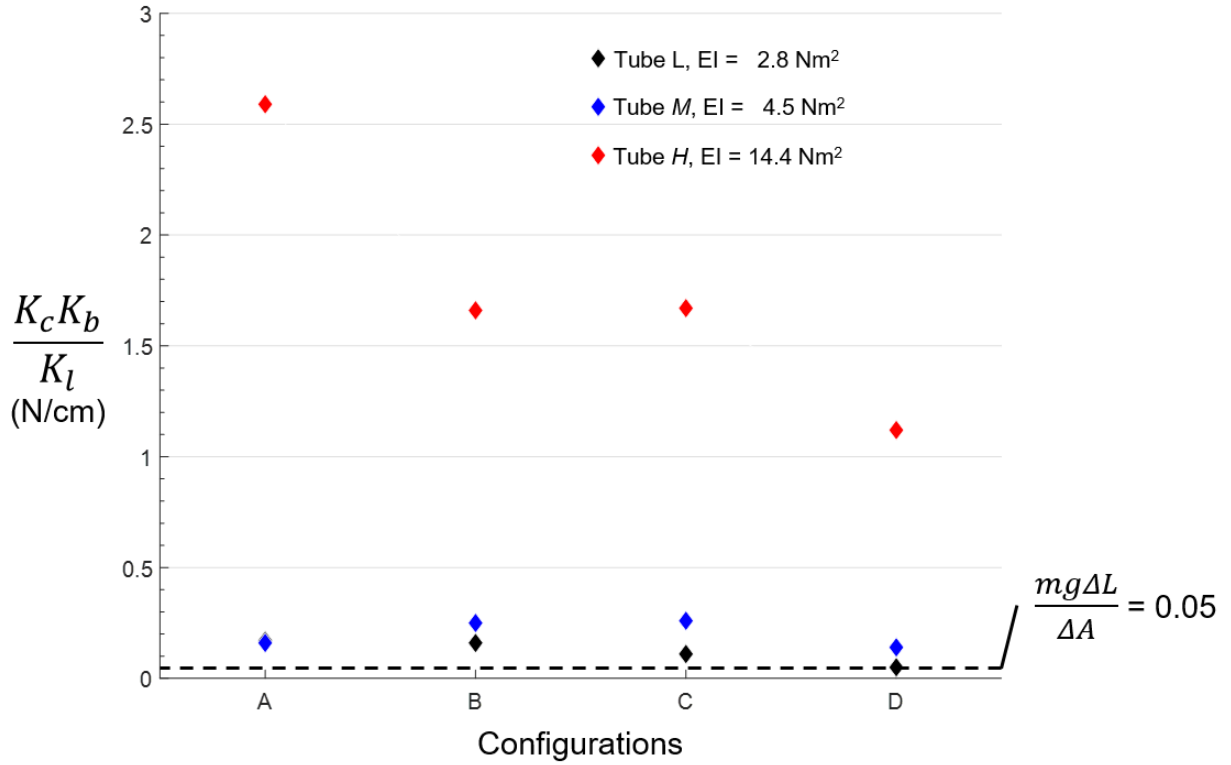
Figure 15: Summary of design criteria as shown in Equation 3. The horizontal dashed line indicates the minimum equivalent stiffness (K_cK_b/K_l) based on mass, change in segment length and change in cross-sectional area ($mg\Delta L/\Delta A$) for peristaltic locomotion for the CMMWorm-S. Tube type 'L', configuration D has an equivalent stiffness of 0.05 N/cm, thus exhibits uneven deformation and poor performance. The other configurations for all tube types are above the desired equivalent stiffness causing increased efficiency in straight-line locomotion.

Biologists have predicted that earthworm body stiffness (resistance to extension) is constant as a function of body mass (Quillin 1999). Since peristaltic locomotion is based on changes in dimensions of the body, longitudinal and circumferential body wall strains are highly dependent on body length. Quillin (1999) observed that large earthworms were crawling at greater absolute speeds compared to smaller earthworms due to longer stroke lengths. We hypothesize that earthworms rely on circumferential body wall strain during straight-line locomotion and bending stiffness during turning. Experiments directed towards measuring body stiffness of earthworms and correlating measured stiffness parameters to worm locomotion will give roboticists a better insight on the parameters required for the development of future peristaltic robots.

Researchers have defined soft robots as composed primarily of materials with moduli in the range of that of soft biological materials (less than 10^9 Pascals) (Rus and Tolley 2015). Implementing properties of a soft body on a robotic platform has been simplified by reducing or grouping degrees of freedom (Menciassi et al. 2004, Lee et al. 2010), and/or by replacing continuously deformable soft bodies with rigid joints (Wang and Yan 2007, Omori et al. 2009). The CMMWorm-S uses 3-D printed rigid vertex pieces as pin-joints to simplify some of the challenges faced in soft-robotics (Kim et al. 2009, Lipson 2014). Even though the structure of this robot includes some relatively rigid pieces, the effective elastic modulus (0.08×10^4 - 0.65×10^4 Pascals) for the robot lies well within the range of soft-robotics. However, for a truly soft robot

to achieve its potential, all hardware used (sensors, actuation, computation, power and communication) must be embedded within the soft body of the robot, resulting in smarter materials (Rus and Tolley 2015).

CMMWorm-S experiences nonlinear strain during locomotion due to nonlinear stiffness (figure 8 and figure 10). An inherent problem observed during locomotion is the physical phenomena of hysteresis. As observed in figure 12, the speed of a softer body is slower than a more rigid structure. The lack of a strong enough return force (springs) or high structural rigidity that allows even contraction throughout the segment causes a difference in the rate of contraction and expansion. This leads to a loss in efficiency during locomotion. In future work, through model-based analysis we can characterize this phenomenon and can develop control schemes that might reduce the effect of hysteresis during locomotion.

In future work, we will also examine the relationship between turning and friction to allow the robot to turn efficiently on surfaces with different coefficients of friction. Throughout this article, we tested turning on a surface with a large coefficient of friction. During turning, the robot experiences slip in the lateral direction. Slip has efficiency costs (Daltorio et al 2013), but we have found that through model-based calibration, slip can be reduced (Huang et al 2017) or even eliminated by making the control waves configuration-dependent (Daltorio 2017). The robot presented in this paper will be ideal for exploring the effect of body softness in new responsive gaits for turning, obstacle avoidance, and confined environments.

Acknowledgements

Appendix A

As the rigid vertex piece composing the rhombus reaches its maximum limit, the tubes start to act like springs causing a sharp change in the slope of the measured extension.
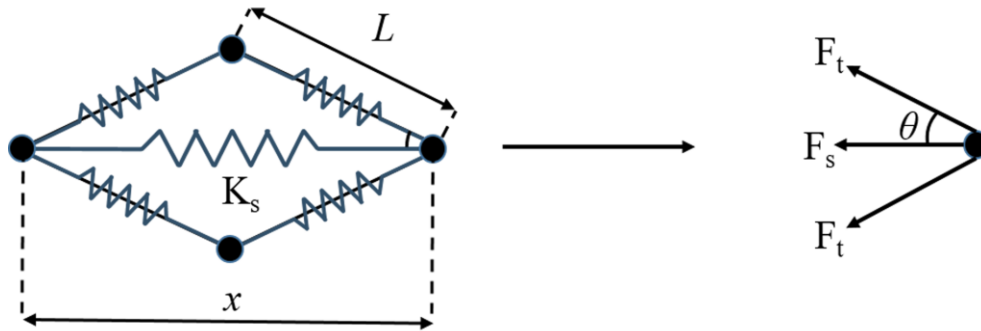

Figure A1: Free body diagram of a vertex piece, showing the forces acting on the right node once the maximum limit angles are reached. F_s is the force due to the spring, while F_t is the force exerted by the tube as if it were a spring. Total extension of the spring (stiffness K_s) is x. L is the rhombus side length and θ is the half-included angle of the rhombus sides.

Total force in horizontal direction:

$$F_{horizontal} = F_s + 2F_t \cos \theta \tag{A1}$$

Where, $F_s = \frac{K_s x}{2}$, $F_t = \frac{K_t x}{2}$ and $\cos \theta = \frac{x}{2L}$

Therefore, total force in horizontal direction:

$$F_{horizontal} = \frac{K_s x}{2} + \frac{K_t x^2}{2L} \qquad (A2)$$

References:

Bertetto, A.M. and Ruggiu, M., 2001. In-pipe inch-worm pneumatic flexible robot. *Proc. IEEE/ASME International Conference on Advanced Intelligent Mechatronics*, Vol. 2, pp. 1226-1231.

Boxerbaum, A.S., Chiel, H.J. and Quinn, R.D., 2010, May. A new theory and methods for creating peristaltic motion in a robotic platform. *Proc. IEEE International Conference on Robotics and Automation*, pp. 1221-1227.

Boxerbaum, A.S., Horchler, A.D., Shaw, K.M., Chiel, H.J. and Quinn, R.D., 2012, May. Worms, waves and robots. *Proc. IEEE International Conference on Robotics and Automation*, pp. 3537-3538.

Chan, B., Ji, S., Koveal, C. and Hosoi, A.E., 2007. Mechanical devices for snail-like locomotion. *Journal of intelligent material systems and structures*, *18*(2), pp.111-116.

Chirikjian, G.S. and Burdick, J.W., 1991, November. Hyper-redundant robot mechanisms and their applications. *Proc. IEEE/RSJ International Workshop on Intelligent Robots and Systems*, pp. 185-190.

Daltorio, K. A., Boxerbaum, A. S., Horchler, A. D., Shaw, K. M., Chiel, H. J. and Quinn, R. D. 2013, Efficient worm-like locomotion: slip and control of soft-bodied peristaltic robots. *Bioinspiriation and Biomimetics.* **8**(3) 035003.

Daltorio, K.A. Kinematics of slip elimination in worm turning. *In prep.*

Dario, P., Ciarletta, P., Menciassi, A. and Kim, B., 2004. Modeling and experimental validation of the locomotion of endoscopic robots in the colon. *The International Journal of Robotics Research*, *23*(4-5), pp.549-556.

Harigaya, K., Adachi, K., Yanagida, T., Yokojima, M. and Nakamura, T., 2013, February. Development of a peristaltic crawling robot for sewer pipe inspection. *Proc. IEEE International Conference on Mechatronics*, pp. 267-272.

Horchler, A. D., 2015a DynamixelQ: Library to control ROBOTIS Dynamixel smart servo actuators with the OpenCM9.04, Ver 1.2 *https://github.com/horchler/DynamixelQ*.

Horchler, A.D., Kandhari, A., Daltorio, K.A., Moses, K.C., Andersen, K.B., Bunnelle, H., Kershaw, J., Tavel, W.H., Bachmann, R.J., Chiel, H.J. and Quinn, R.D., 2015b. Worm-like robotic locomotion with a compliant modular mesh. In *Conference on Biomimetic and Biohybrid Systems, Living Machines*, pp. 26-37.

Horchler, A.D., Kandhari, A., Daltorio, K.A., Moses, K.C., Ryan, J.C., Stultz, K.A., Kanu, E.N., Andersen, K.B., Kershaw, J.A., Bachmann, R.J. and Chiel, H.J., 2015c. Peristaltic locomotion of a modular mesh-based worm robot: precision, compliance, and friction. *Soft Robotics*, *2*(4), pp.135-145.

Huang, Y., Kandhari, A., Chiel, H.J., Quinn, R.D. and Daltorio, K.A., 2017 Slip Reduction Controls of Mesh-Body Worm Robot Developed from a Mathematical Model. *2017 IEEE ROBIO*. Accepted, in press.

Ikeuchi, M., Nakamura, T. and Matsubara, D., 2012, October. Development of an in-pipe inspection robot for narrow pipes and elbows using pneumatic artificial muscles. *Proc. IEEE/RSJ International Conference on Intelligent Robots and Systems*, pp. 926-931.

Kim, D., Park, S., Mahadevan, L. and Shin, J.H., 2011. The shallow turn of a worm. *Journal of Experimental Biology*, *214*(9), pp.1554-1559.

Kim, S., Laschi, C. and Trimmer, B., 2013. Soft robotics: a bioinspired evolution in robotics. *Trends in biotechnology*, *31*(5), pp.287-294.

Lee, E., Yang, J., Jolda, M. and Wood, R., 2010. Cellular slime mold robot. In *the International Conference on Robotics and Automation*, pp. 30-35.

Lipson, H., 2014. Challenges and opportunities for design, simulation, and fabrication of soft robots. *Soft Robotics*, *1*(1), pp.21-27.

Mangan, E.V., Kingsley, D.A., Quinn, R.D. and Chiel, H.J., 2002. Development of a peristaltic endoscope. *Proc. IEEE International Conference on Robotics and Automation*, Vol. 1, pp. 347-352.

Menciassi, A., Gorini, S., Pernorio, G. and Dario, P., 2004, April. A SMA actuated artificial earthworm. *Proc. IEEE International Conference on Robotics and Automation*, Vol. 4, pp. 3282-3287.

Omori, H., Hayakawa, T. and Nakamura, T., 2008, September. Locomotion and turning patterns of a peristaltic crawling earthworm robot composed of flexible units. *Proc. IEEE/RSJ International Conference on Intelligent Robots and Systems*, pp. 1630-1635.

Omori, H., Nakamura, T. and Yada, T., 2009. An underground explorer robot based on peristaltic crawling of earthworms. *Industrial Robot: An International Journal*, *36*(4), pp.358-364.

Omori, H., Nakamura, T., Iwanaga, T. and Hayakawa, T., 2010. Development of mobile robots based on peristaltic crawling of an earthworm. In *Robotics 2010 current and future challenges*. InTech, pp. 299-319.

Onal, C.D. and Rus, D., 2012, June. A modular approach to soft robots. *Proc. IEEE RAS and EMBS International Conference on Biomedical Robotics and Biomechatronics*, pp. 1038-1045.

Quillin, K.J., 1999. Kinematic scaling of locomotion by hydrostatic animals: ontogeny of peristaltic crawling by the earthworm lumbricus terrestris. *Journal of Experimental Biology*, *202*(6), pp.661-674.

Rus, D. and Tolley, M.T., 2015. Design, fabrication and control of soft robots. *Nature*, *521*(7553), pp.467.

Seok, S., Onal, C.D., Cho, K.J., Wood, R.J., Rus, D. and Kim, S., 2013. Meshworm: a peristaltic soft robot with antagonistic nickel titanium coil actuators. *IEEE/ASME Transactions on mechatronics*, *18*(5), pp.1485-1497.

Tanaka, T., Harigaya, K. and Nakamura, T., 2014 Development of a peristaltic crawling robot for long-distance inspection of sewer pipes. *Proc. IEEE/ASME International Conference on Advanced Intelligent Mechatronics*, *pp. 1552-1557.*

Trimmer, B.A., Takesian, A.E., Sweet, B.M., Rogers, C.B., Hake, D.C. and Rogers, D.J., 2006, May. Caterpillar locomotion: a new model for soft-bodied climbing and burrowing robots. *International Symposium on Technology and the Mine Problem*, Vol. 1, pp. 1-10.

Trivedi, D., Rahn, C.D., Kier, W.M. and Walker, I.D., 2008. Soft robotics: Biological inspiration, state of the art, and future research. *Applied Bionics and Biomechanics*, *5*(3), pp.99-117.

Umedachi, T. and Trimmer, B.A., 2014, May. Design of a 3D-printed soft robot with posture and steering control. *Proc. IEEE International Conference on Robotics and Automation*, pp. 2874-2879.

Wang, K. and Yan, G., 2007. Micro robot prototype for colonoscopy and in vitro experiments. *Journal of medical engineering and technology*, *31*(1), pp.24-28.